Observation of quasi-planar boron carbonyl complexes $B_{36}(CO)_n^+$ (n = 1-6) analogous to coronene monocation $C_{24}H_{12}^+$

Table of Contents

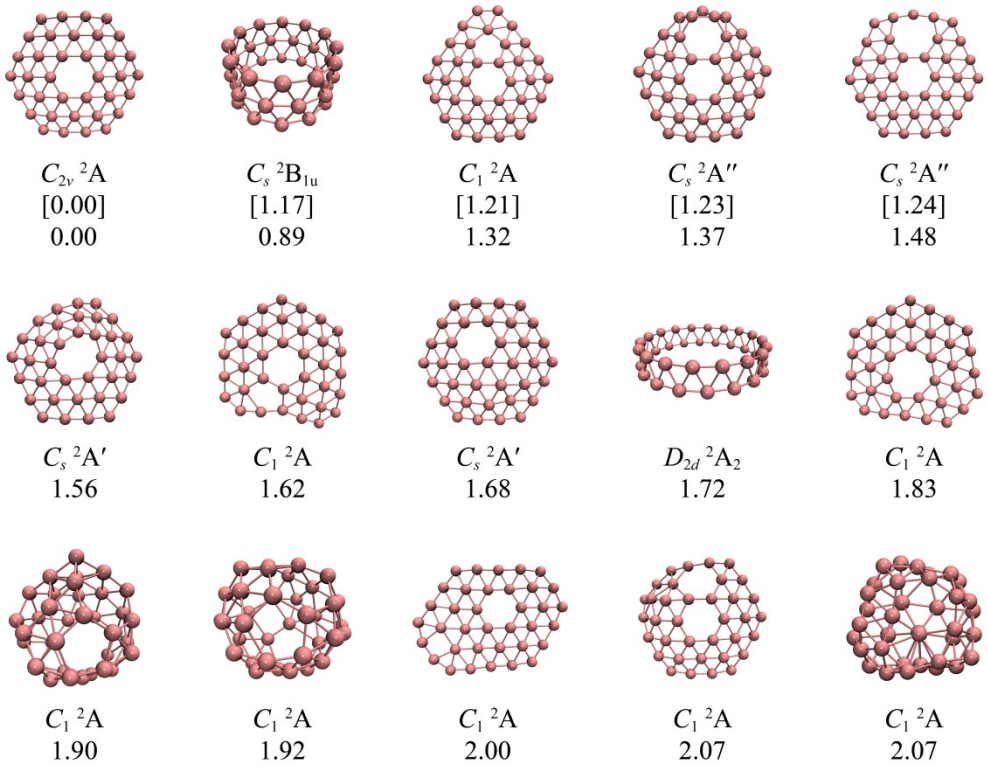

Fig.S1 Optimized low-lying isomers of B_{36}^+, with the relative energies indicated in eV at DLPNO-CCSD(T)/def2-svp in square brackets and PBE0/6-311+G(d).

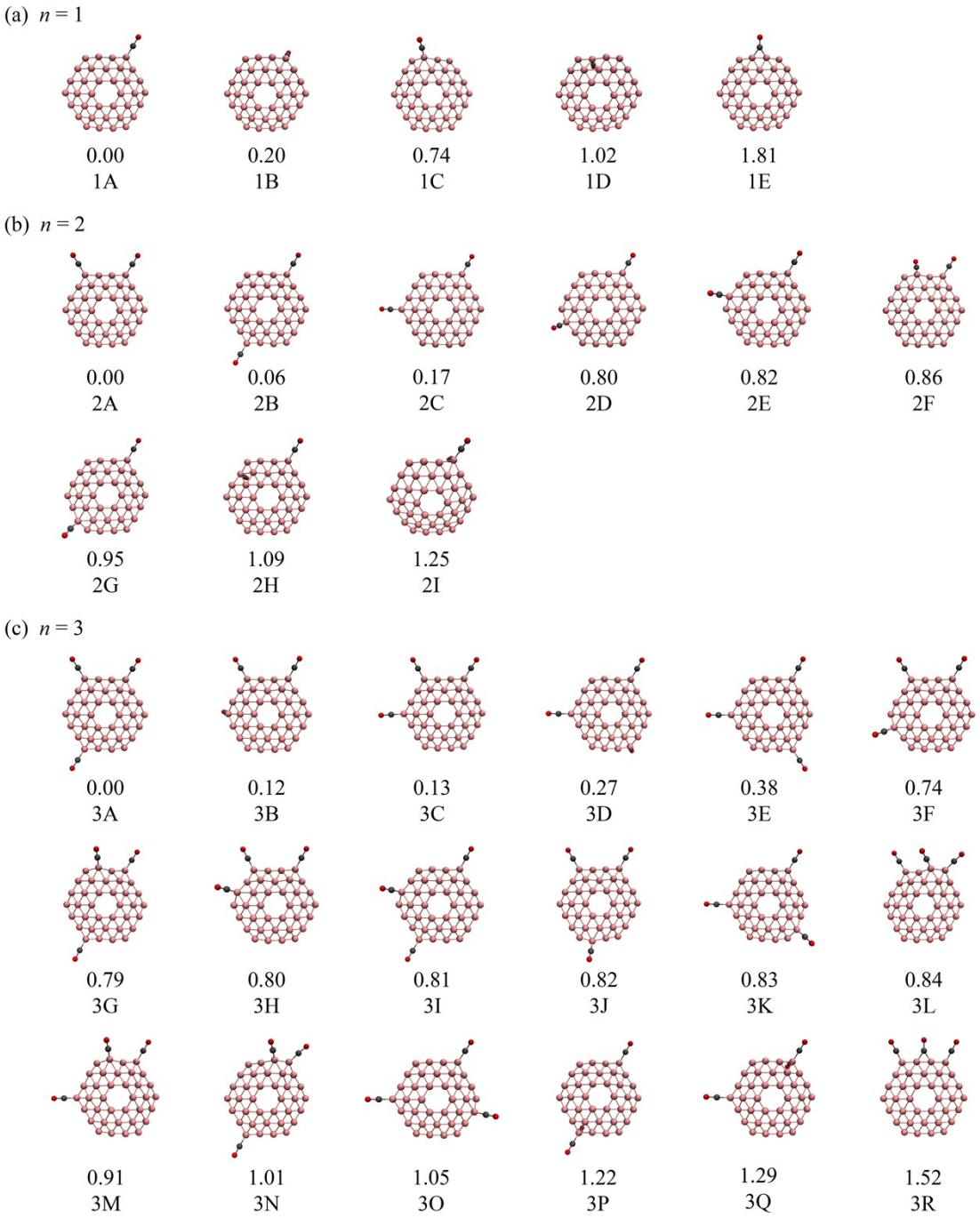

Fig.S2 Optimized low-lying isomers of $B_{36}(CO)_n^+$ (n = 1-3) at PBE0-D3/6-311+G(d) level, with the relative energies (ΔE) indicated in eV.

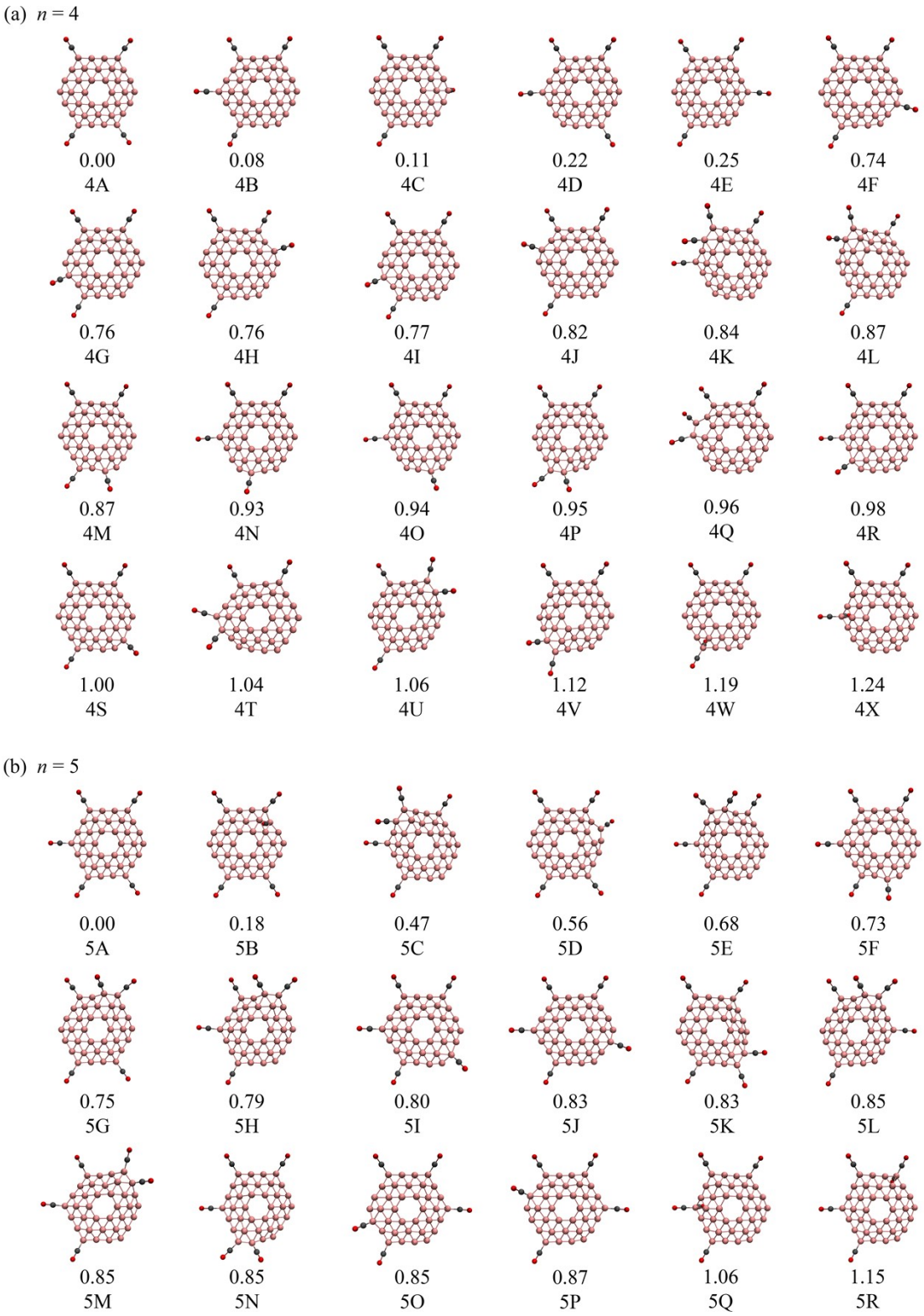

Fig.S3 Optimized low-lying isomers of $B_{36}(CO)_n^+$ (n = 4, 5) at PBE0-D3/6-311+G(d) level, with the relative energies (ΔE) indicated in eV.

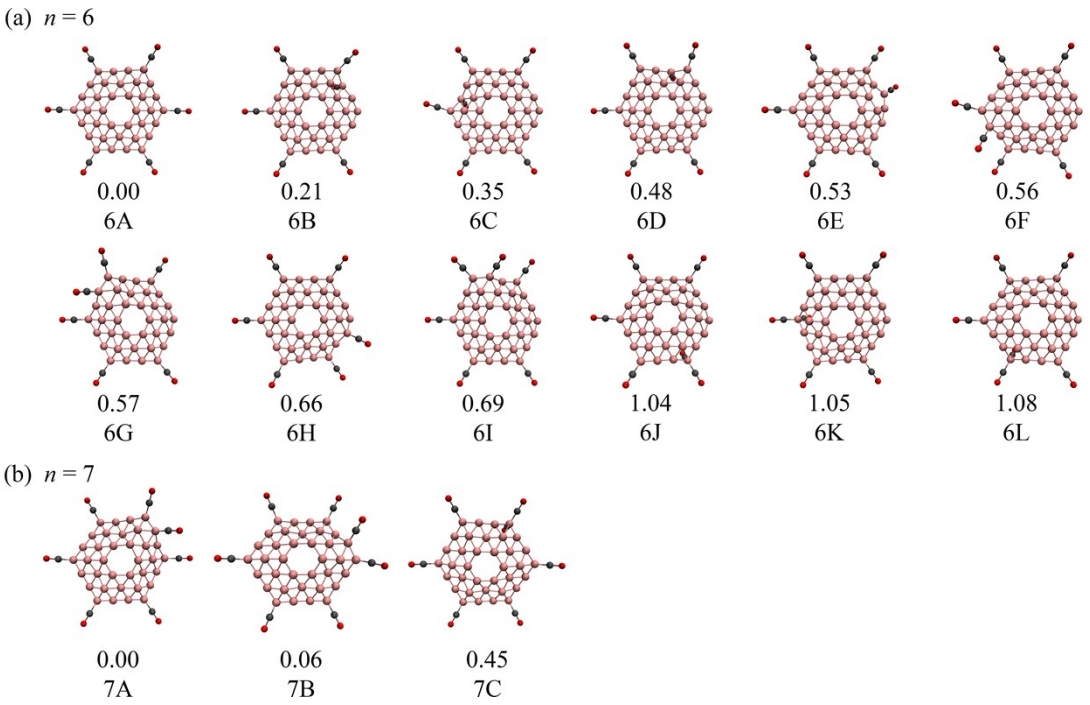

Fig.S4 Optimized low-lying isomers of $B_{36}(CO)_n^+$ (n = 6, 7) at PBE0-D3/6-311+G(d) level, with the relative energies (ΔE) indicated in eV.

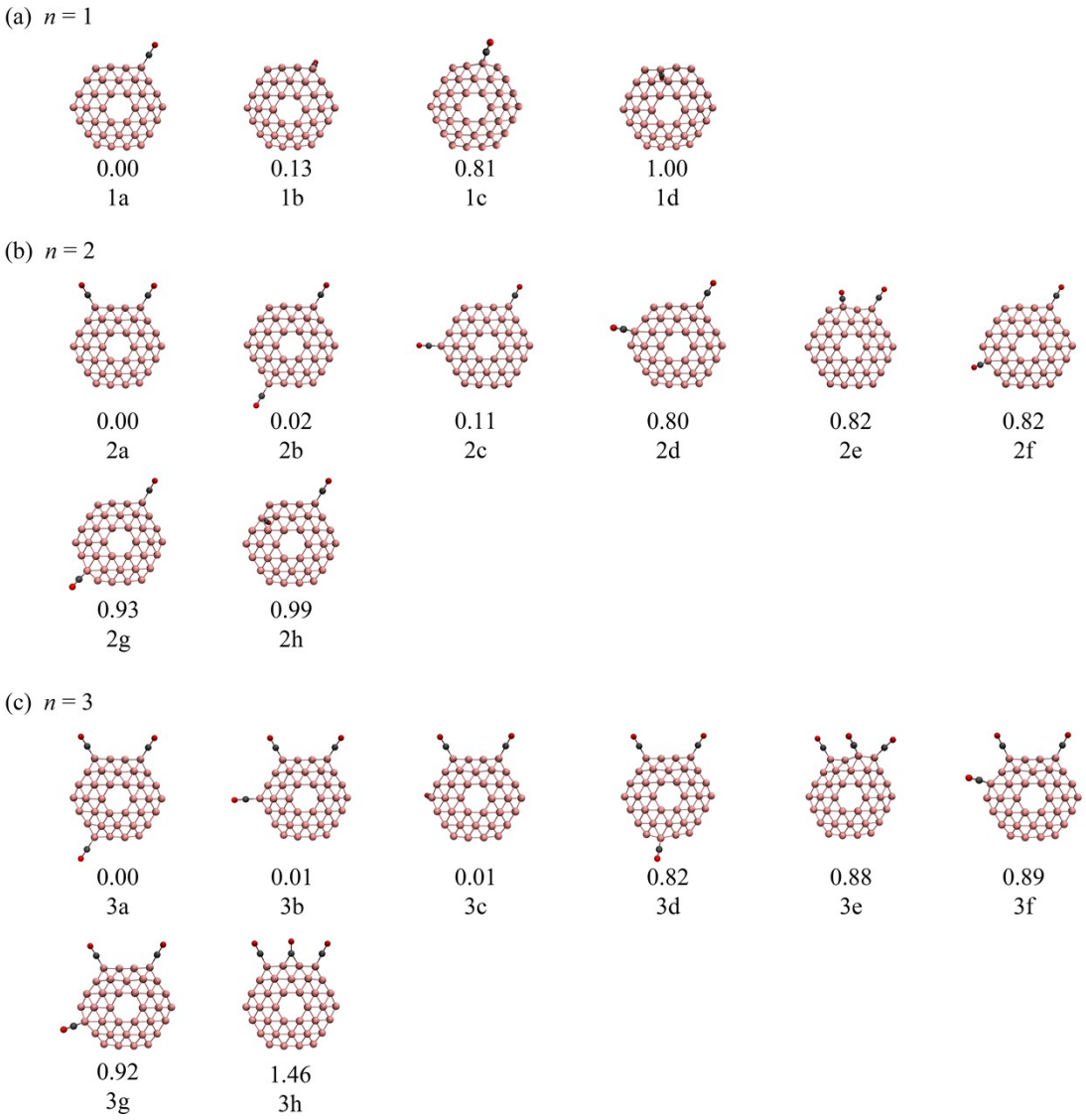

Fig.S5 Optimized low-lying isomers of $B_{36}(CO)_n$ (n = 1-3) at PBE0-D3/6-311+G(d) level, with the relative energies (ΔE) indicated in eV.

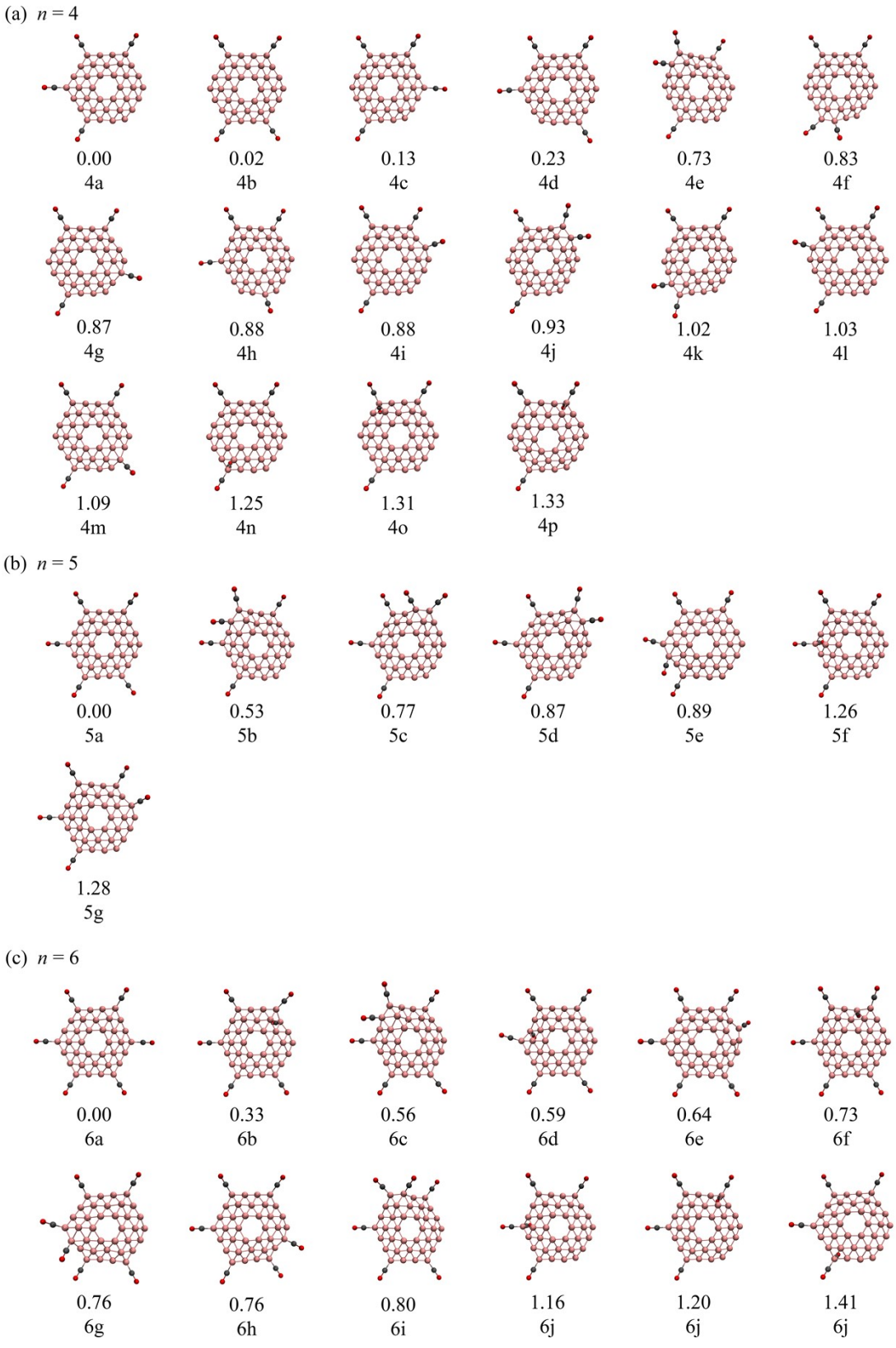

Fig.S6 Optimized low-lying isomers of $B_{36}(CO)_n$ (n = 4-6) at PBE0-D3/6-311+G(d) level, with the relative energies (ΔE) indicated in eV.

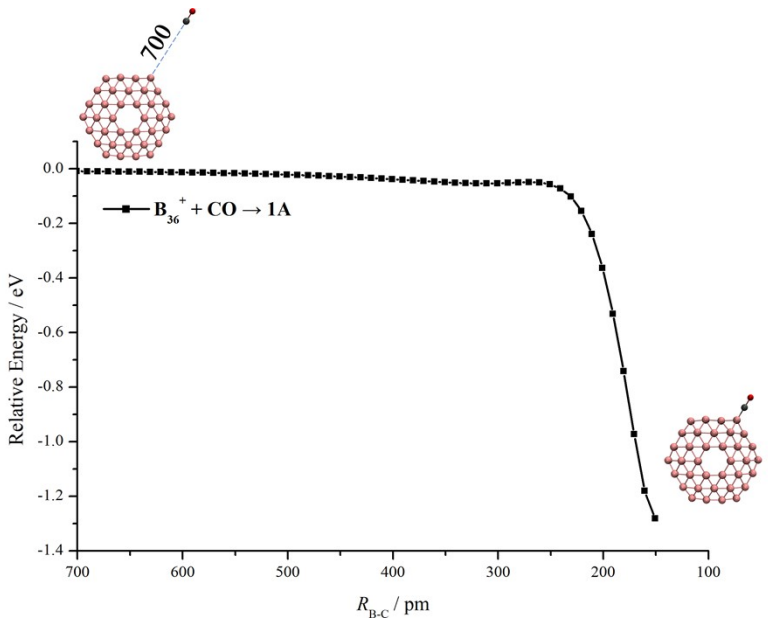

Fig.S7 Calculated relaxed potential energy curves for the approach of CO toward B_{36}^+ to form $B_{36}CO^+$ (1a) at PBE0/6-311+G(d), with the B–CO distances indicated in pm.

(a)

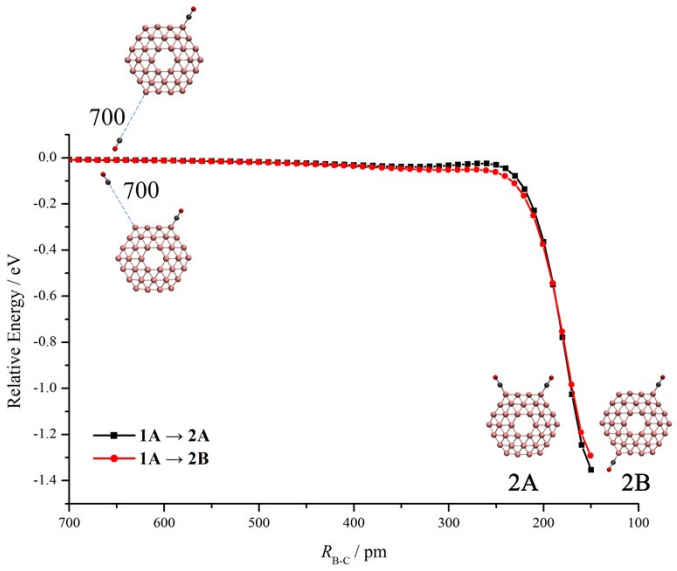

(b)

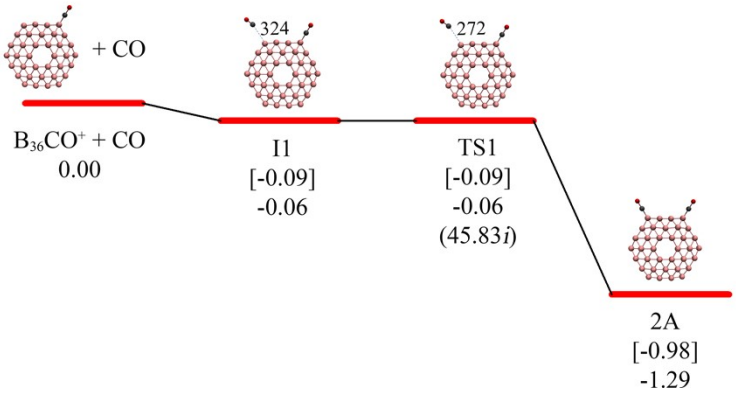

Fig.S8 (a) Calculated relaxed potential energy curves for the approach of CO toward $B_{36}CO^+$(**1A**) to form $B_{36}(CO)_2^+$(**2A**, **2B**) at PBE0/6-311+G(d). (b) Potential energy profile for the formation of **2A** and **2B** from **1A** and CO, calculated at the PBE0-D3/6-311+G(d) level of theory. The profile indicates the B–CO distances (in pm) and the imaginary vibrational frequency of TS1 (in cm^{-1}), with all values including zero-point energy corrections. The relative energies in square brackets are from DLPNO-CCSD(T)/def2-SVP single-point calculations on the PBE0-D3/6-311+G(d) optimized structures.

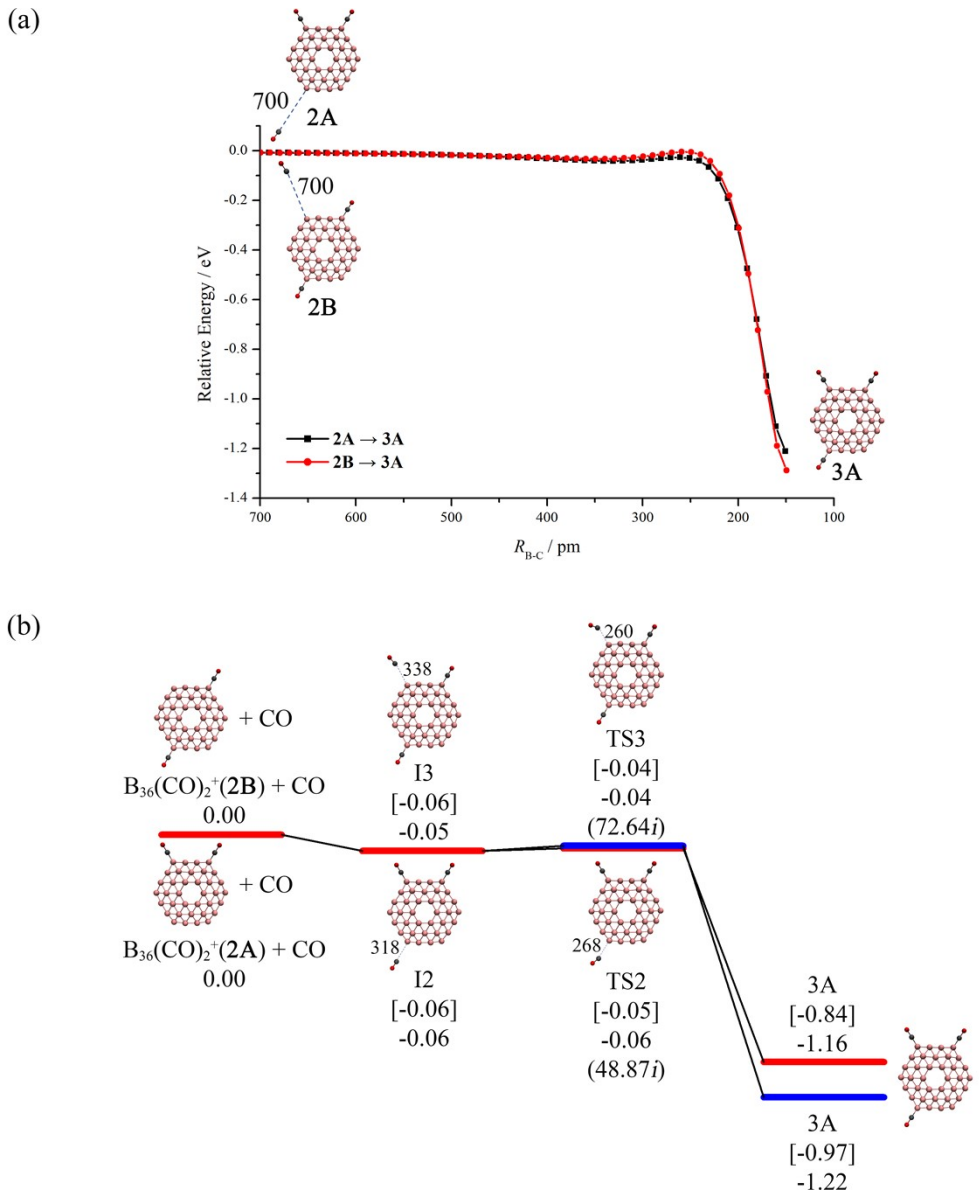

Fig.S9 (a) Calculated relaxed potential energy curves for the approach of CO toward $B_{36}(CO)_2^+$(**2A**, **2B**) to form $B_{36}(CO)_3^+$(**3A**) at PBE0/6-311+G(d). (b) Potential energy profile for the formation of **3A** from a mixture of **2A** and **2B** with CO, calculated at the PBE0-D3/6-311+G(d) level of theory. The profile indicates the B–CO distances (in pm) and the imaginary vibrational frequency of TS2 and TS3 (in cm^{-1}), with all values including zero-point energy corrections. The relative energies in square brackets are from DLPNO-CCSD(T)/def2-SVP single-point calculations on the PBE0-D3/6-311+G(d) optimized structures.

(a)

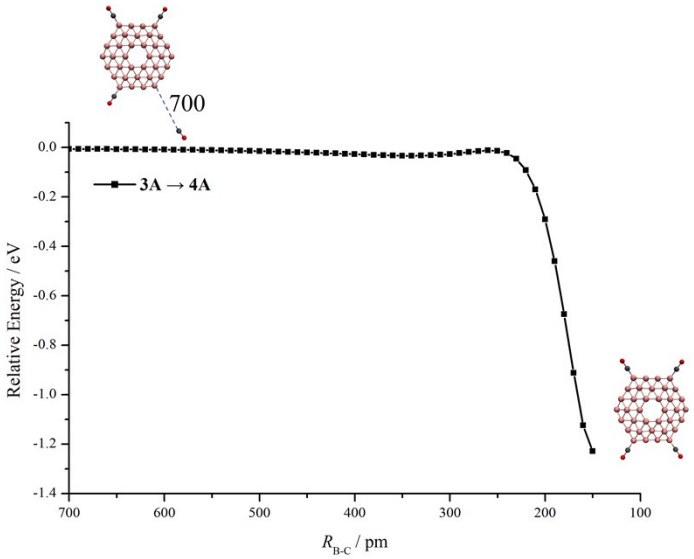

(b)

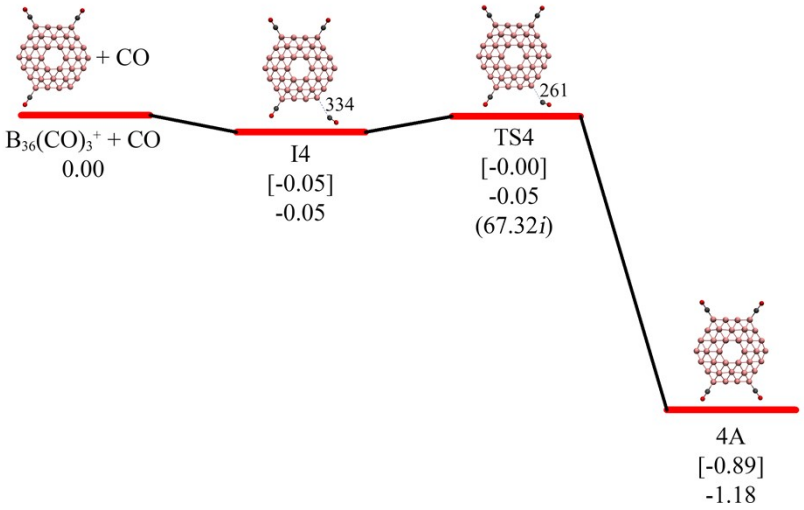

Fig.S10 (a) Calculated relaxed potential energy curves for the approach of CO toward $B_{36}(CO)_3^+$(**3A**) to form $B_{36}(CO)_4^+$(**4A**) at PBE0/6-311+G(d). (b) Potential energy profile for the formation of **4A** from **3A** and CO, calculated at the PBE0-D3/6-311+G(d) level of theory. The profile indicates the B–CO distances (in pm) and the imaginary vibrational frequency of TS4 (in cm^{-1}), with all values including zero-point energy corrections. The relative energies in square brackets are from DLPNO-CCSD(T)/def2-SVP single-point calculations on the PBE0-D3/6-311+G(d) optimized structures.

(a)

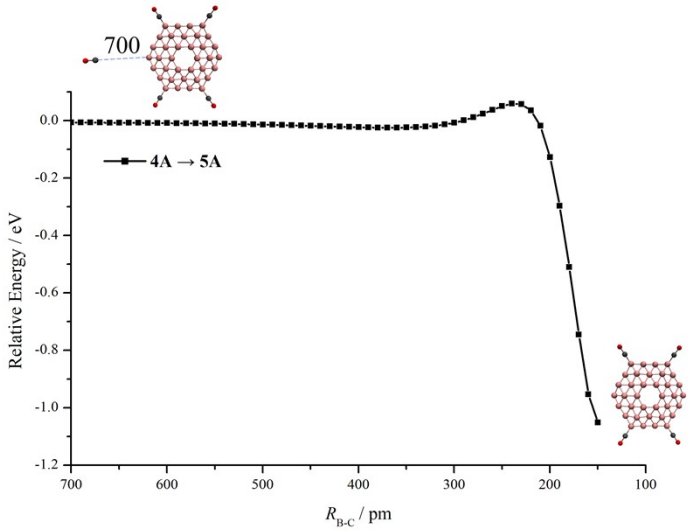

(b)

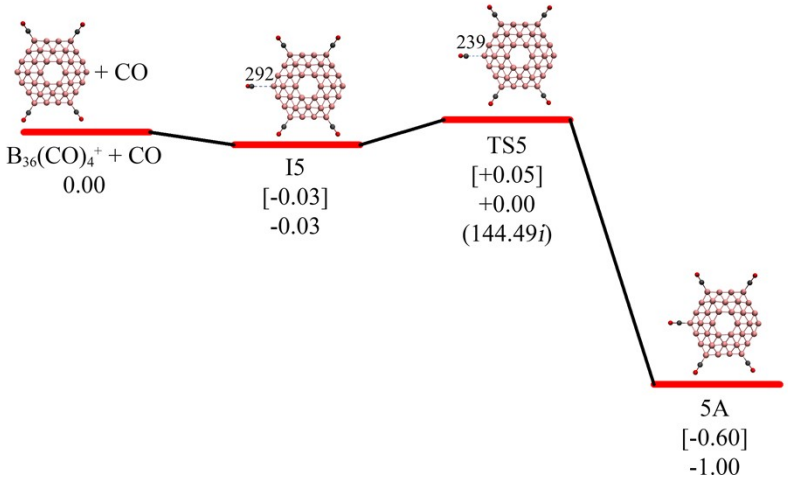

Fig.S11 (a) Calculated relaxed potential energy curves for the approach of CO toward $B_{36}(CO)_4^+$(**4A**) to form $B_{36}(CO)_5^+$(**5A**) at PBE0/6-311+G(d). (b) Potential energy profile for the formation of **5A** from **4A** and CO, calculated at the PBE0-D3/6-311+G(d) level of theory. The profile indicates the B–CO distances (in pm) and the imaginary vibrational frequency of TS5 (in cm^{-1}), with all values including zero-point energy corrections. The relative energies in square brackets are from DLPNO-CCSD(T)/def2-SVP single-point calculations on the PBE0-D3/6-311+G(d) optimized structures.

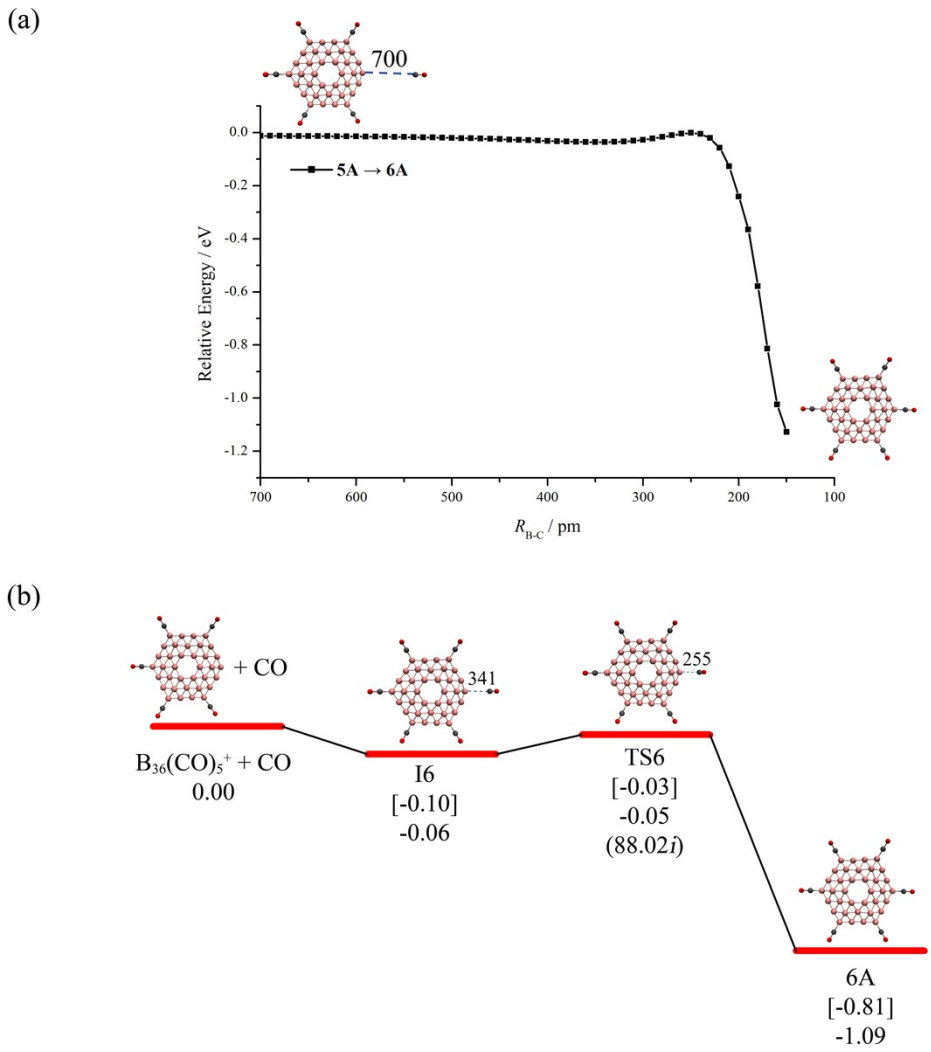

Fig.S12 (a) Calculated relaxed potential energy curves for the approach of CO toward $B_{36}(CO)_5^+$(**5A**) to form $B_{36}(CO)_6^+$(**6A**) at PBE0/6-311+G(d). (b) Potential energy profile for the formation of **6A** from **5A** and CO, calculated at the PBE0-D3/6-311+G(d) level of theory. The profile indicates the B–CO distances (in pm) and the imaginary vibrational frequency of TS6 (in cm^{-1}), with all values including zero-point energy corrections. The relative energies in square brackets are from DLPNO-CCSD(T)/def2-SVP single-point calculations on the PBE0-D3/6-311+G(d) optimized structures.

(a)

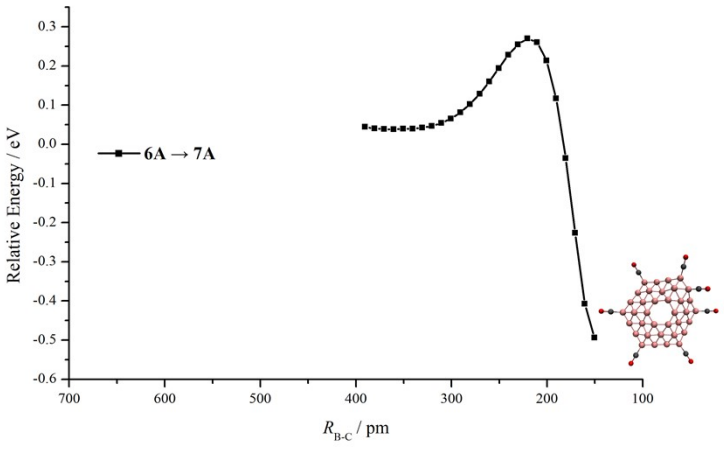

(b)

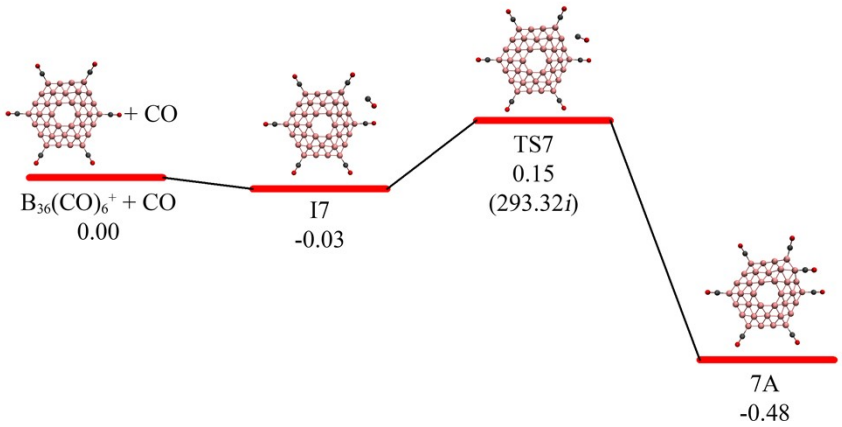

Fig.S13 (a) Calculated relaxed potential energy curves for the approach of CO toward $B_{36}(CO)_6^+$(**6A**) to form $B_{36}(CO)_7^+$(**7A**) at PBE0/6-311+G(d). (b) Potential energy profile for the formation of **7A** from **6A** and CO, calculated at the PBE0-D3/6-311+G(d) level of theory. The profile indicates the B–CO distances (in pm) and the imaginary vibrational frequency of TS7 (in cm^{-1}), with all values including zero-point energy corrections.

(a)

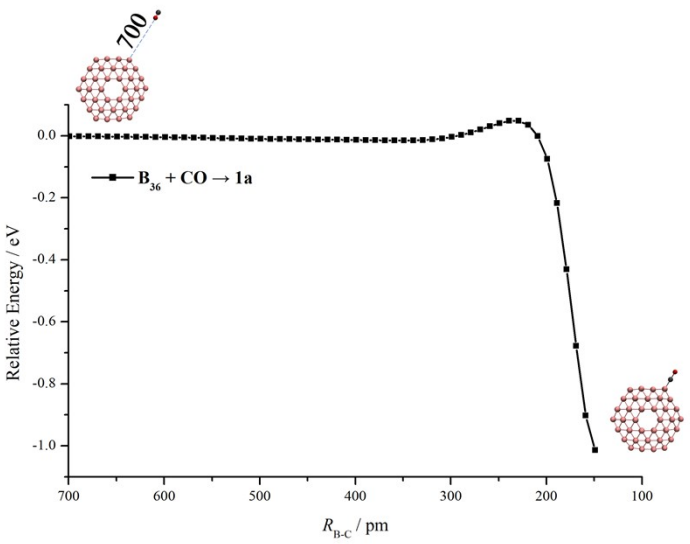

(b)

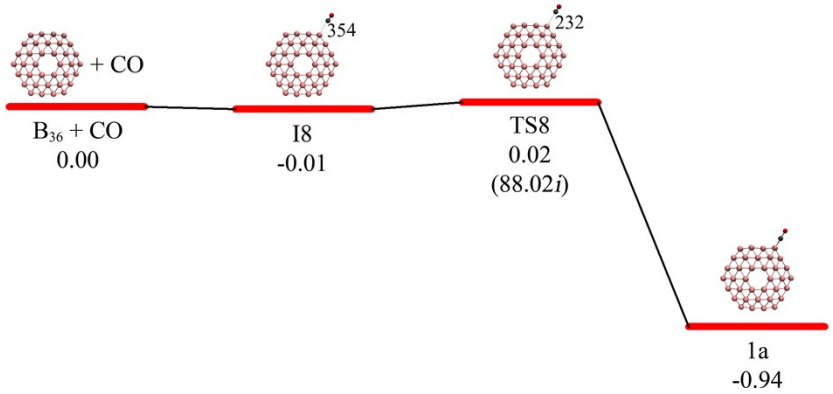

Fig.S14 (a) Calculated relaxed potential energy curves for the approach of CO toward B_{36} to form $B_{36}CO$ (**1a**) at PBE0/6-311+G(d). (b) Potential energy profile for the formation of **1a** from B_{36} and CO, calculated at the PBE0-D3/6-311+G(d) level of theory. The profile indicates the B–CO distances (in pm) and the imaginary vibrational frequency of TS8 (in cm^{-1}), with all values including zero-point energy corrections.

(a)

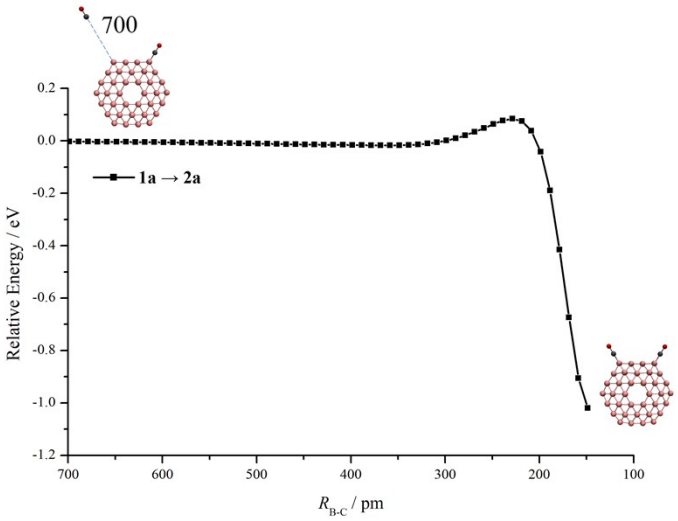

(b)

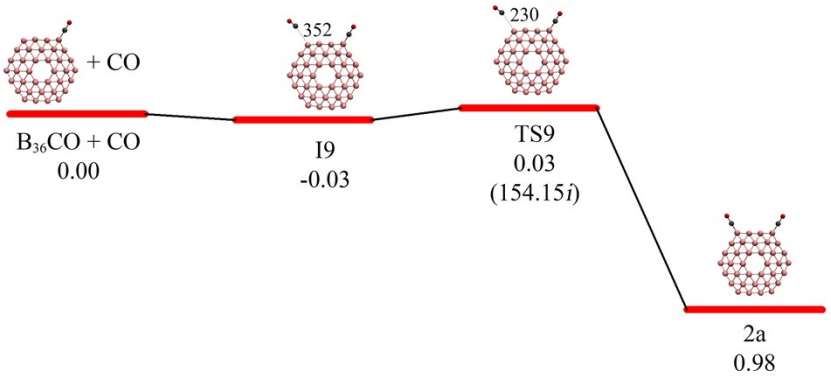

Fig.S15 (a) Calculated relaxed potential energy curves for the approach of CO toward $B_{36}CO$ (**1a**) to form $B_{36}(CO)_2$ (**2a**) at PBE0/6-311+G(d). (b) Potential energy profile for the formation of **2a** from **1a** and CO, calculated at the PBE0-D3/6-311+G(d) level of theory. The profile indicates the B–CO distances (in pm) and the imaginary vibrational frequency of TS9 (in cm^{-1}), with all values including zero-point energy corrections.

(a)

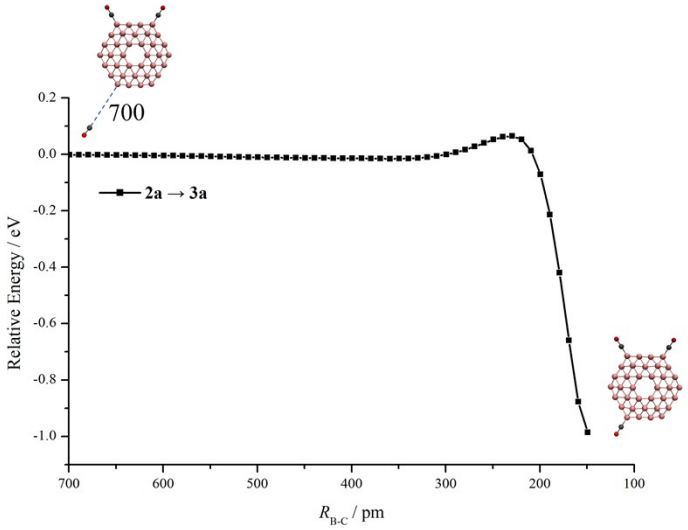

(b)

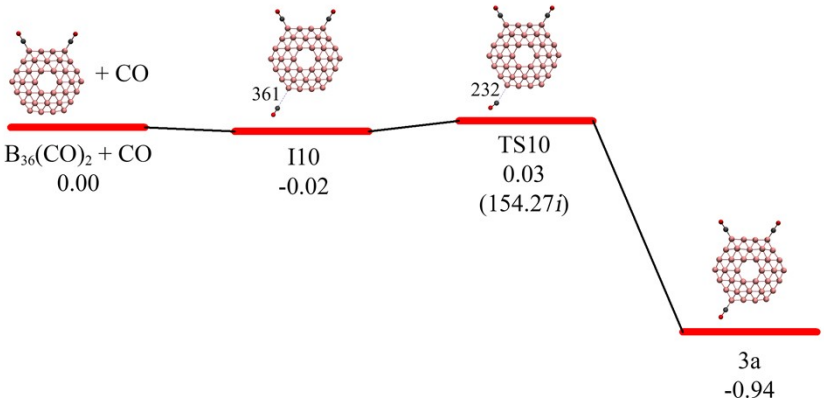

Fig.S16 (a) Calculated relaxed potential energy curves for the approach of CO toward $B_{36}(CO)_2$ (**2a**) to form $B_{36}(CO)_3$ (**3a**) at PBE0/6-311+G(d). (b) Potential energy profile for the formation of **3a** from **2a** and CO, calculated at the PBE0-D3/6-311+G(d) level of theory. The profile indicates the B–CO distances (in pm) and the imaginary vibrational frequency of TS10 (in cm^{-1}), with all values including zero-point energy corrections.

(a)

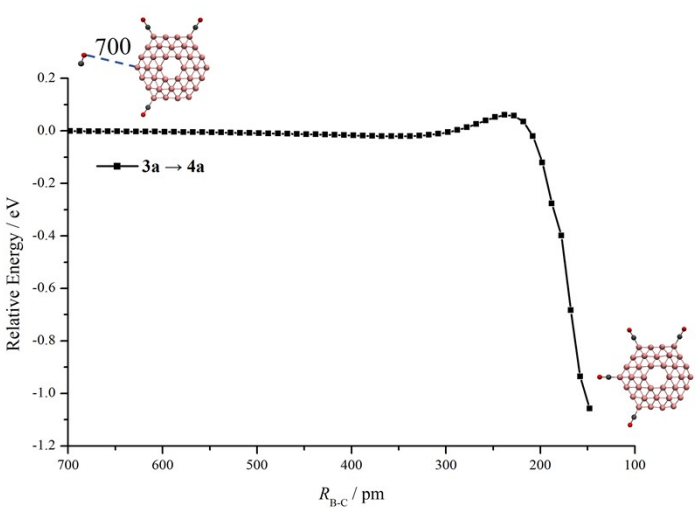

(b)

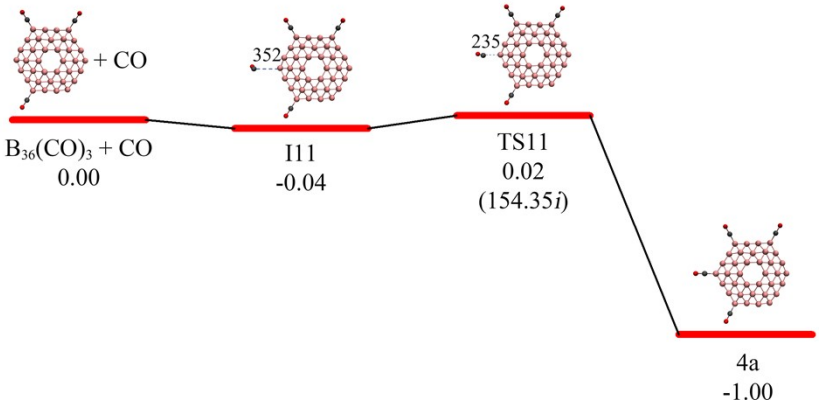

Fig.S17 (a) Calculated relaxed potential energy curves for the approach of CO toward $B_{36}(CO)_3$ (**3a**) to form $B_{36}(CO)_4$ (**4a**) at PBE0/6-311+G(d). (b) Potential energy profile for the formation of **4a** from **3a** and CO, calculated at the PBE0-D3/6-311+G(d) level of theory. The profile indicates the B–CO distances (in pm) and the imaginary vibrational frequency of TS11 (in cm^{-1}), with all values including zero-point energy corrections.

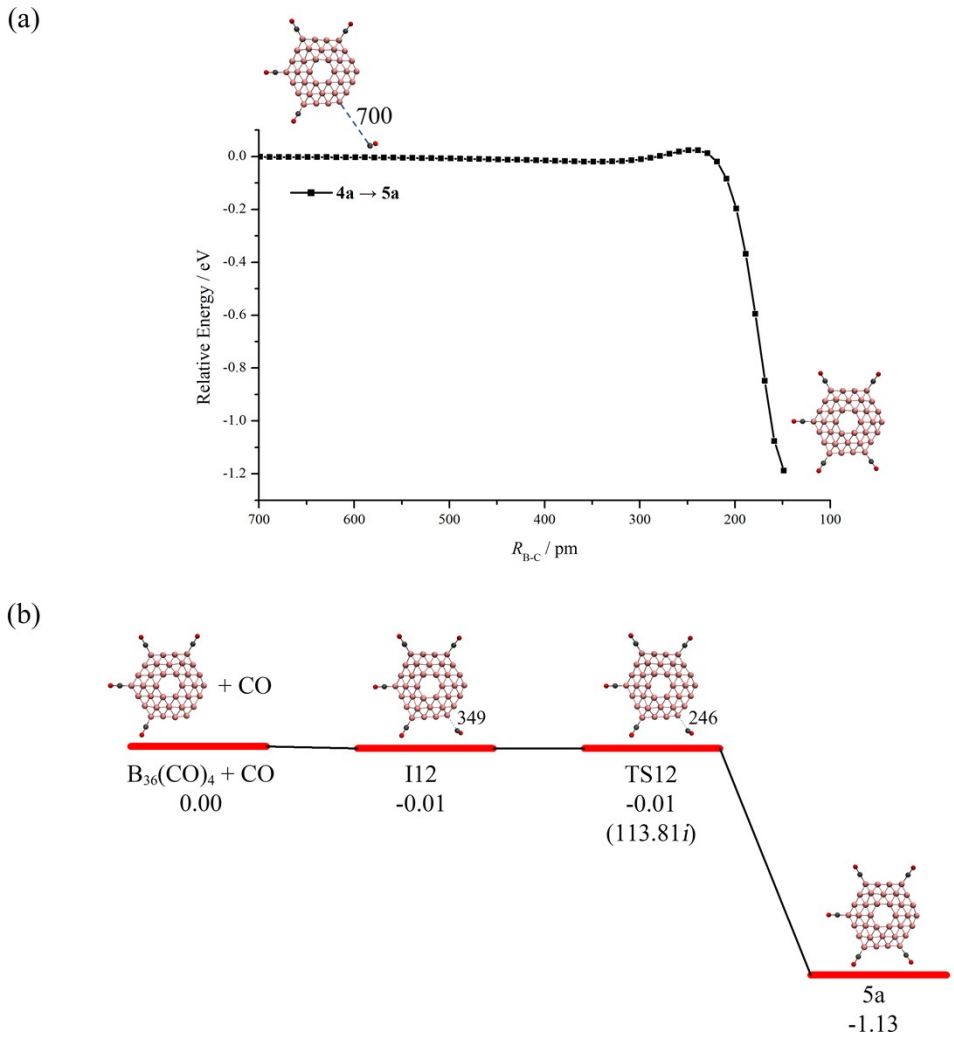

Fig.S18 (a) Calculated relaxed potential energy curves for the approach of CO toward $B_{36}(CO)_4$ (**4a**) to form $B_{36}(CO)_5$ (**5a**) at PBE0/6-311+G(d). (b) Potential energy profile for the formation of **5a** from **4a** and CO, calculated at the PBE0-D3/6-311+G(d) level of theory. The profile indicates the B–CO distances (in pm) and the imaginary vibrational frequency of TS12 (in cm^{-1}), with all values including zero-point energy corrections.

(a)

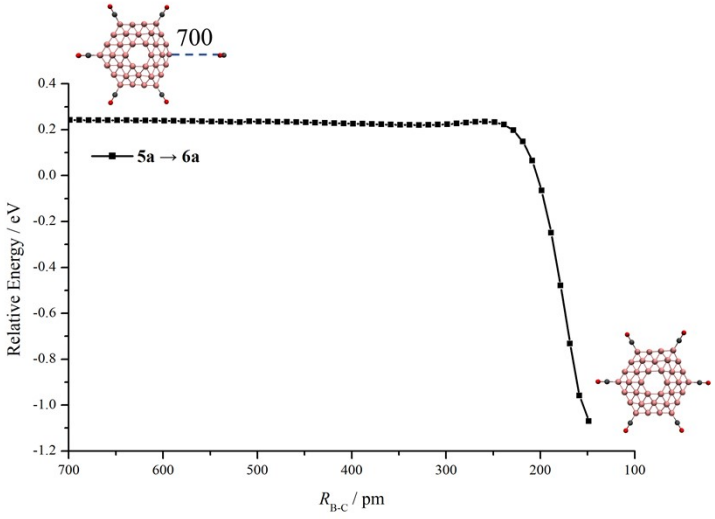

(b)

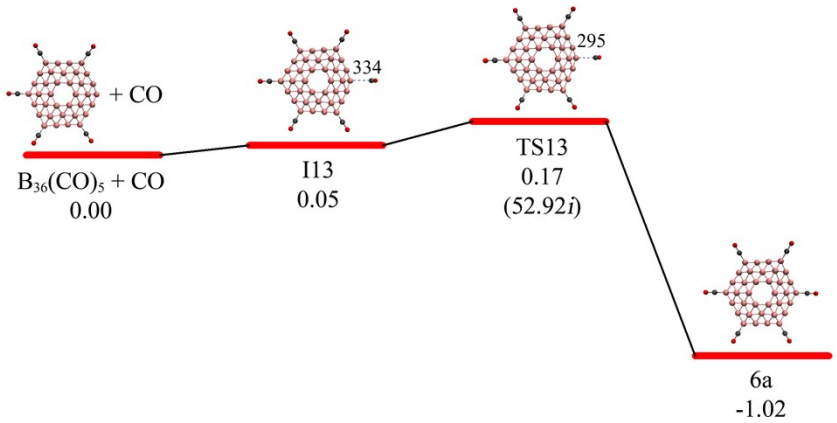

Fig.S19 (a) Calculated relaxed potential energy curves for the approach of CO toward $B_{36}(CO)_5$ (**6a**) to form $B_{36}(CO)_6$ (**6a**) at PBE0/6-311+G(d). (b) Potential energy profile for the formation of **6a** from **5a** and CO, calculated at the PBE0-D3/6-311+G(d) level of theory. The profile indicates the B–CO distances (in pm) and the imaginary vibrational frequency of TS13 (in cm^{-1}), with all values including zero-point energy corrections.

(a) C_s $B_{36}CO^+$ (1A)

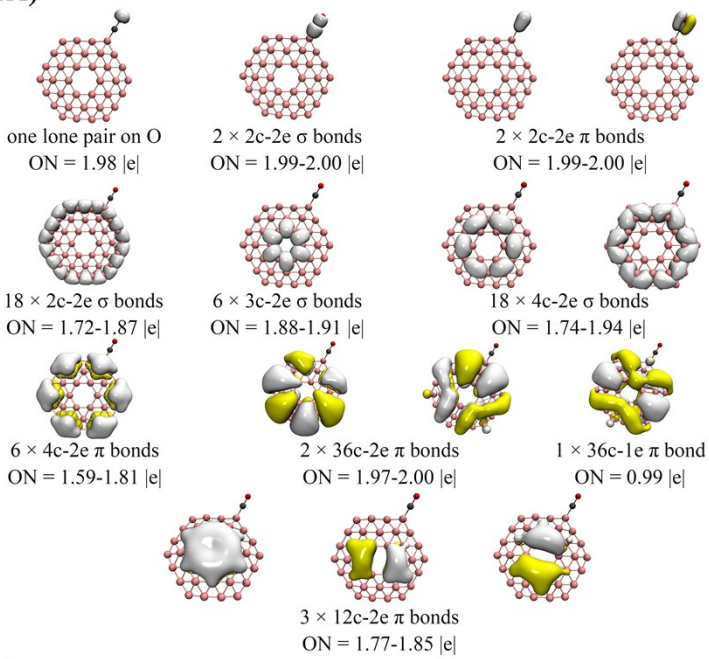

(b) C_{2v} $B_{36}(CO)_2^+$ (2A)

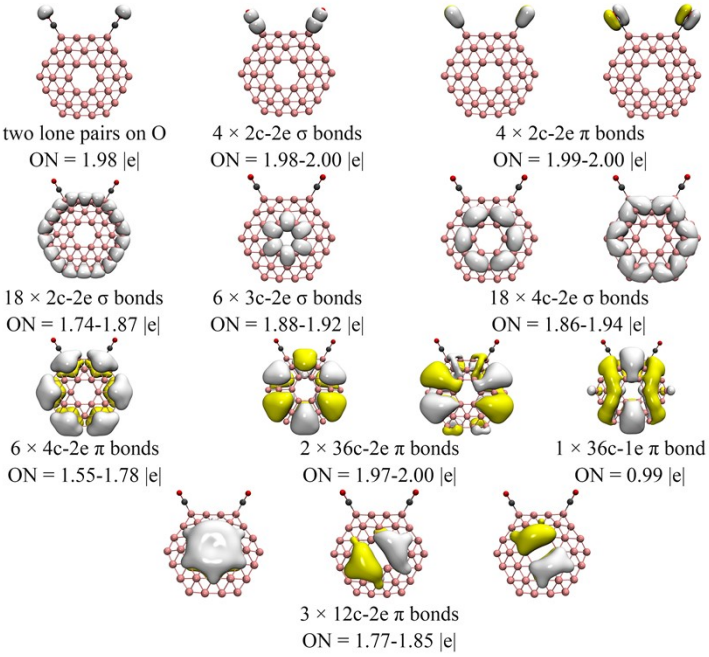

Fig.S20 AdNDP bonding patterns of (a) C_s $B_{36}CO^+$ (**1A**) and (b) C_{2v} $B_{36}(CO)_2^+$ (**2A**), with the occupation numbers (ONs) indicated.

(a) C_1 $B_{36}(CO)_3^+$ (3A)

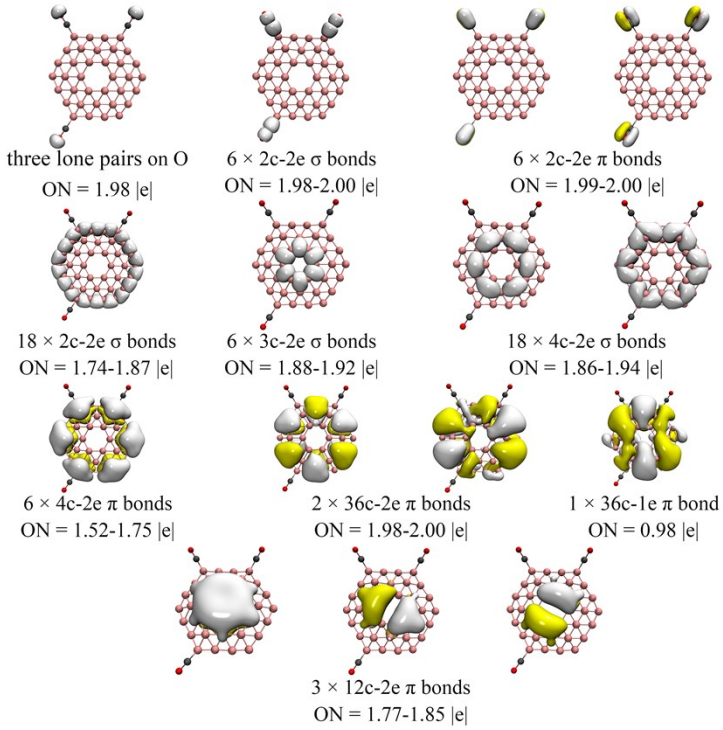

(b) C_{2v} $B_{36}(CO)_4^+$ (4A)

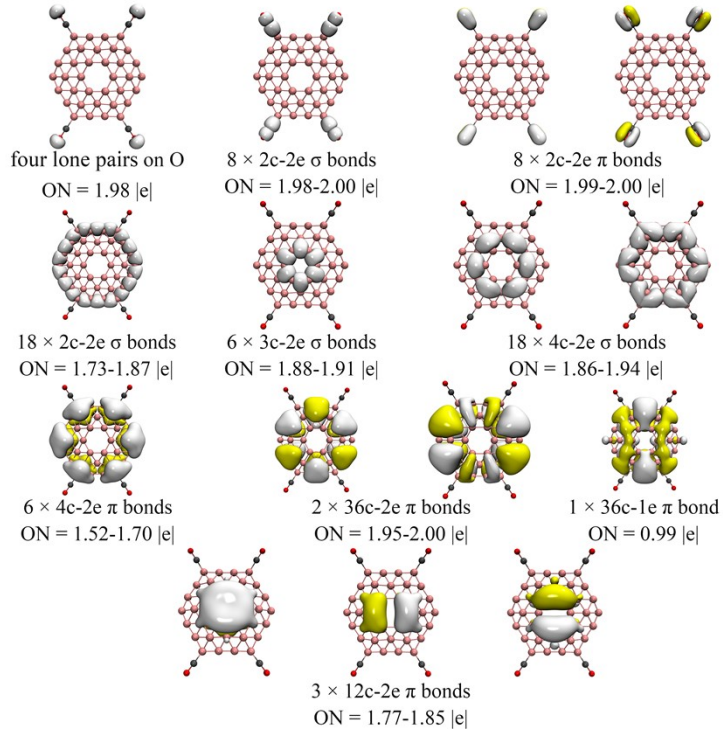

Fig.S21 AdNDP bonding patterns of (a) C_1 $B_{36}(CO)_3^+$ (**3A**) and (b) C_{2v} $B_{36}(CO)_4^+$ (**4A**), with the occupation numbers (ONs) indicated.

(a) C_s $B_{36}(CO)_5^+$ (5A)

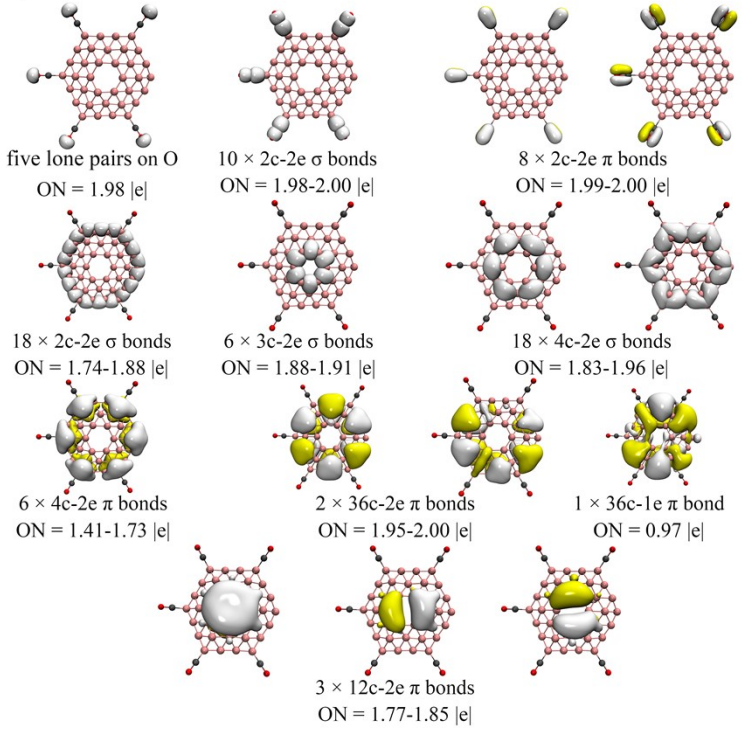

(b) C_s $B_{36}(CO)_6^+$ (6A)

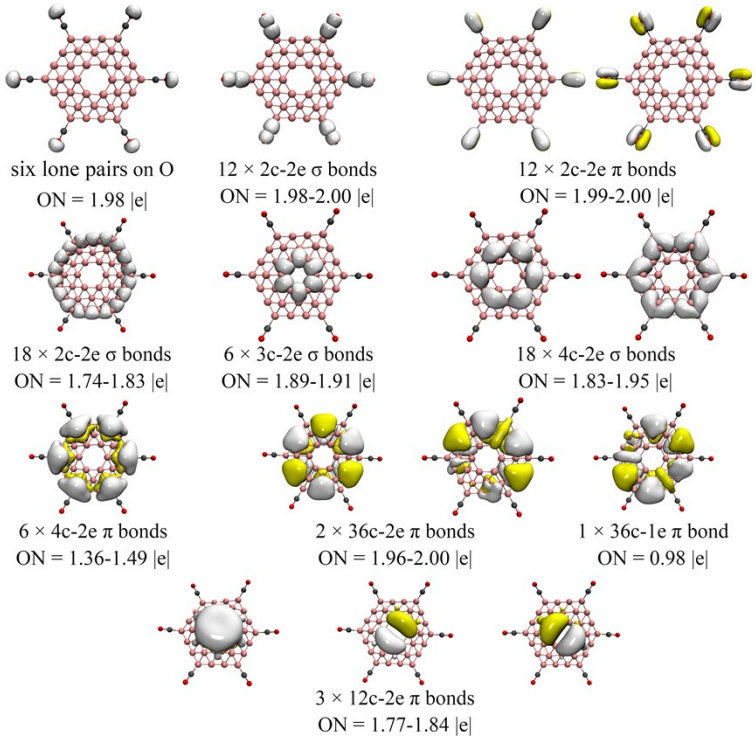

Fig.S22 AdNDP bonding patterns of (a) C_s $B_{36}(CO)_5^+$ (**5A**) and (b) C_s $B_{36}(CO)_6^+$ (**6A**), with the occupation numbers (ONs) indicated.

(a) C_s $B_{36}CO$ (1a)

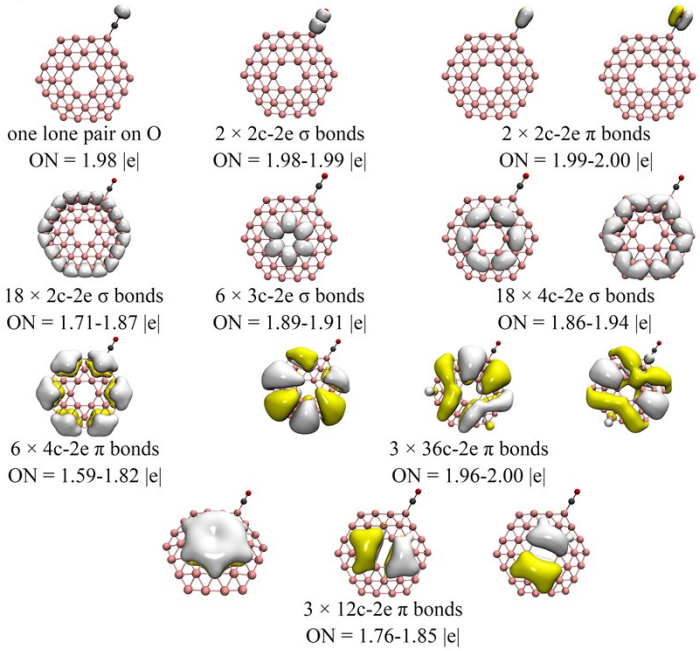

(b) C_s $B_{36}(CO)_2$ (2a)

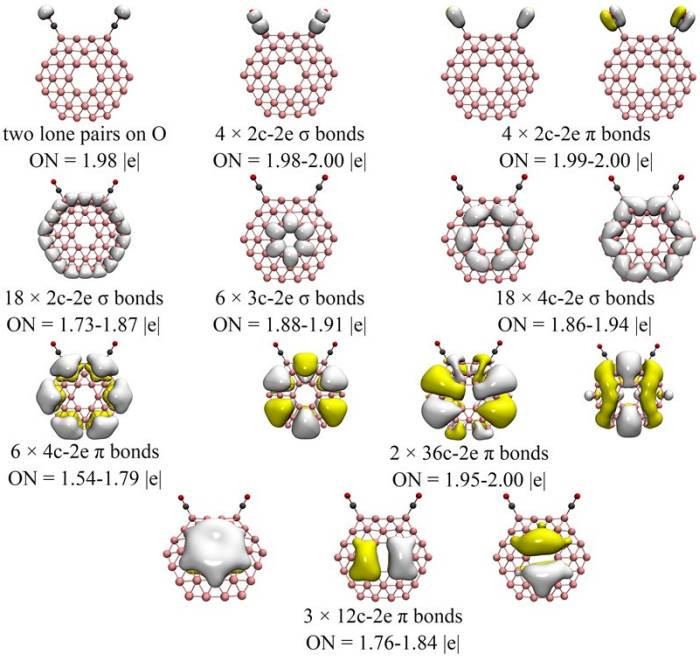

Fig.S23 AdNDP bonding patterns of (a) C_s $B_{36}CO$ (**1a**) and (b) C_s $B_{36}(CO)_2$ (**2a**), with the occupation numbers (ONs) indicated.

(a) C_1 $B_{36}(CO)_3$ (3a)

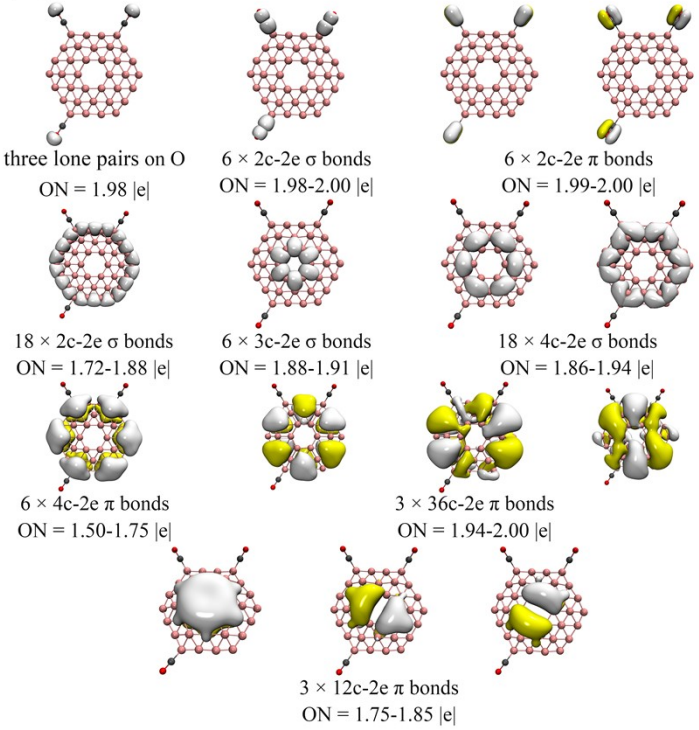

(b) C_1 $B_{36}(CO)_4$ (4a)

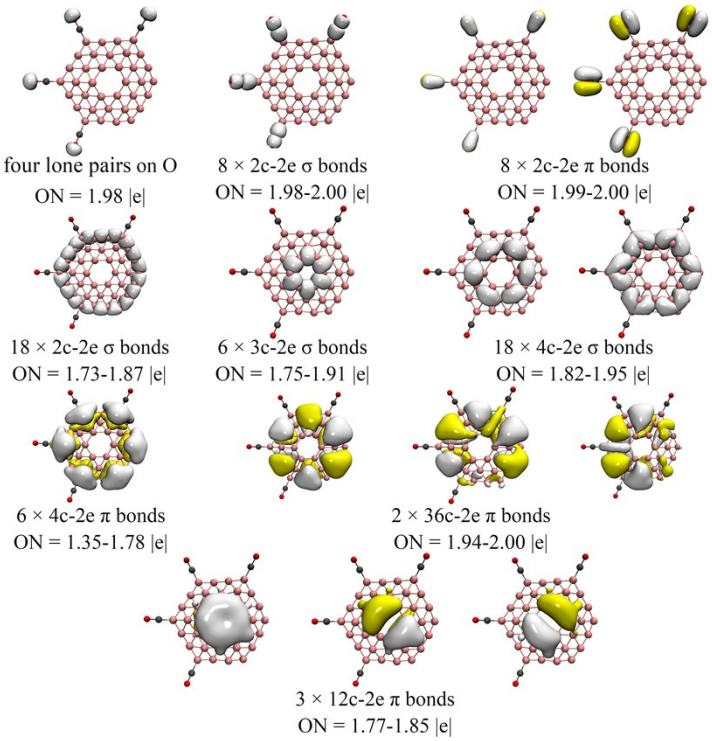

Fig.S24 AdNDP bonding patterns of (a) C_1 $B_{36}(CO)_3$ (**3a**) and (b) C_1 $B_{36}(CO)_4$ (**4a**), with the occupation numbers (ONs) indicated.

(a) C_s $B_{36}(CO)_5$ (5a)

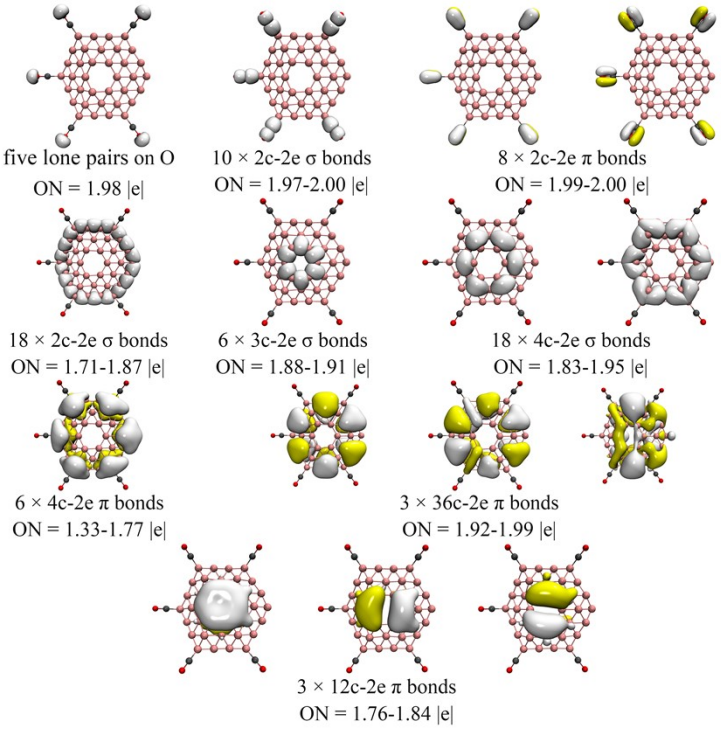

(b) C_{3v} $B_{36}(CO)_6$ (6a)

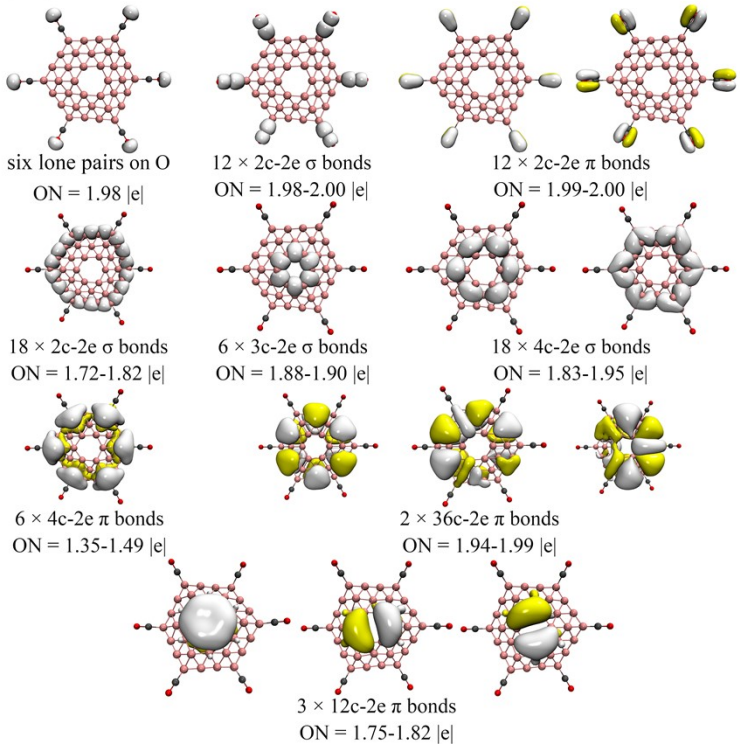

Fig.S25 AdNDP bonding patterns of (a) C_s $B_{36}(CO)_5$ (**5a**) and (b) C_{3v} $B_{36}(CO)_6$ (**6a**), with the occupation numbers (ONs) indicated.

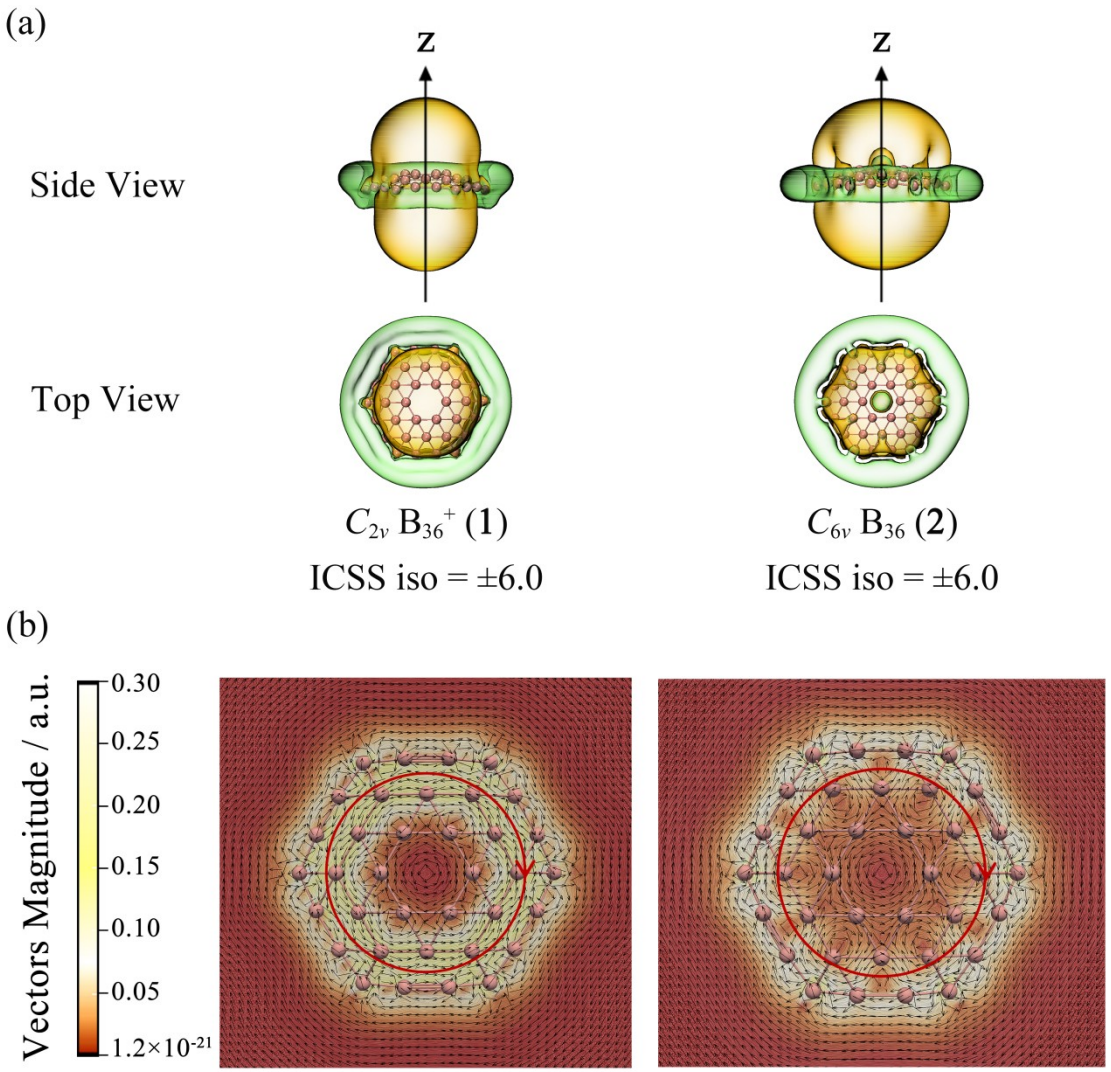

Fig.S26 (a) Calculated ICSS surfaces of C_{2v} B_{36}^{+} (**1**), C_{6v} B_{36} (**2**) at PBE0 level. Yellow and green regions stand for chemical shielding and de-shielding areas, respectively. (b) The corresponding calculated GIMIC plots 1.0 Å above the molecular planes, with the calculated ring current densities indicated in a.u. in the colour scale. The external magnetic field is perpendicular to the molecular plane. The red arrows represent directions of the ring currents on the GIMIC iso-surfaces.

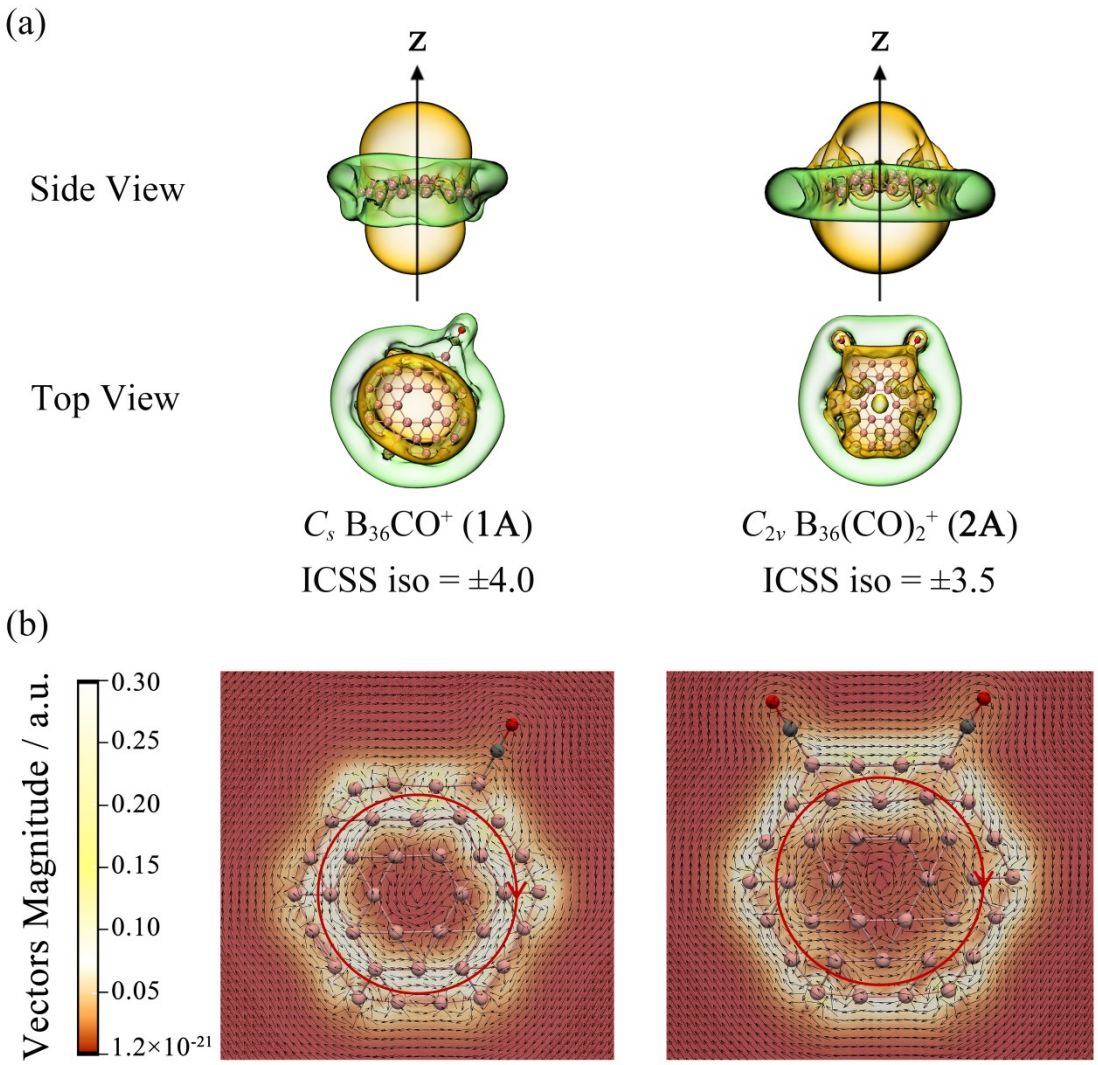

Fig.S27 (a) Calculated ICSS surfaces of C_s $B_{36}CO^+$ (**1A**), C_{2v} $B_{36}(CO)_2^+$ (**2A**) at PBE0 level. Yellow and green regions stand for chemical shielding and de-shielding areas, respectively. (b) The corresponding calculated GIMIC plots 1.0 Å above the molecular planes, with the calculated ring current densities indicated in a.u. in the colour scale. The external magnetic field is perpendicular to the molecular plane. The red arrows represent directions of the ring currents on the GIMIC iso-surfaces.

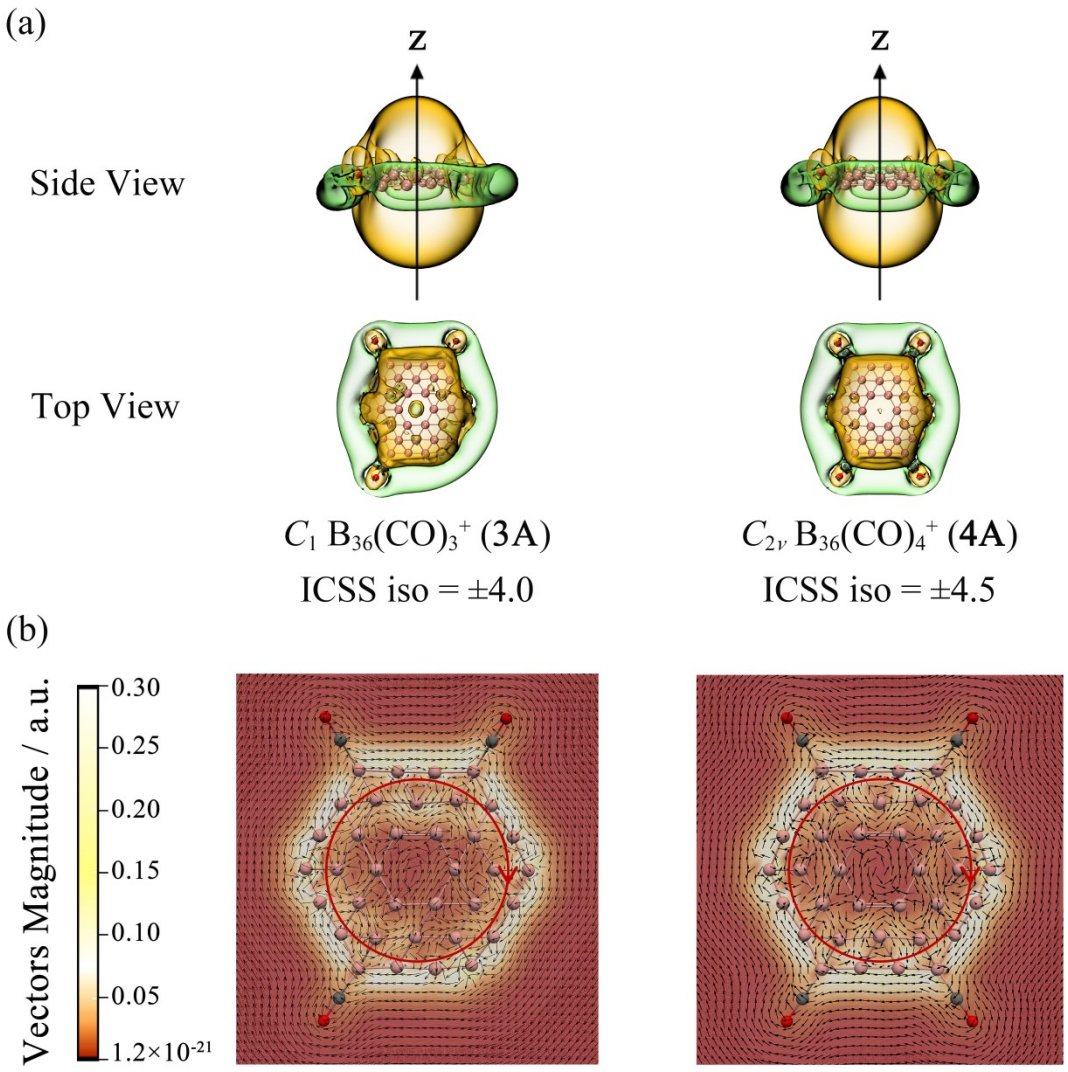

Fig.S28 (a) Calculated ICSS surfaces of C_1 $B_{36}(CO)_3^+$ (**3A**), C_{2v} $B_{36}(CO)_4^+$ (**4A**) at PBE0 level. Yellow and green regions stand for chemical shielding and de-shielding areas, respectively. (b) The corresponding calculated GIMIC plots 1.0 Å above the molecular planes, with the calculated ring current densities indicated in a.u. in the colour scale. The external magnetic field is perpendicular to the molecular plane. The red arrows represent directions of the ring currents on the GIMIC iso-surfaces.

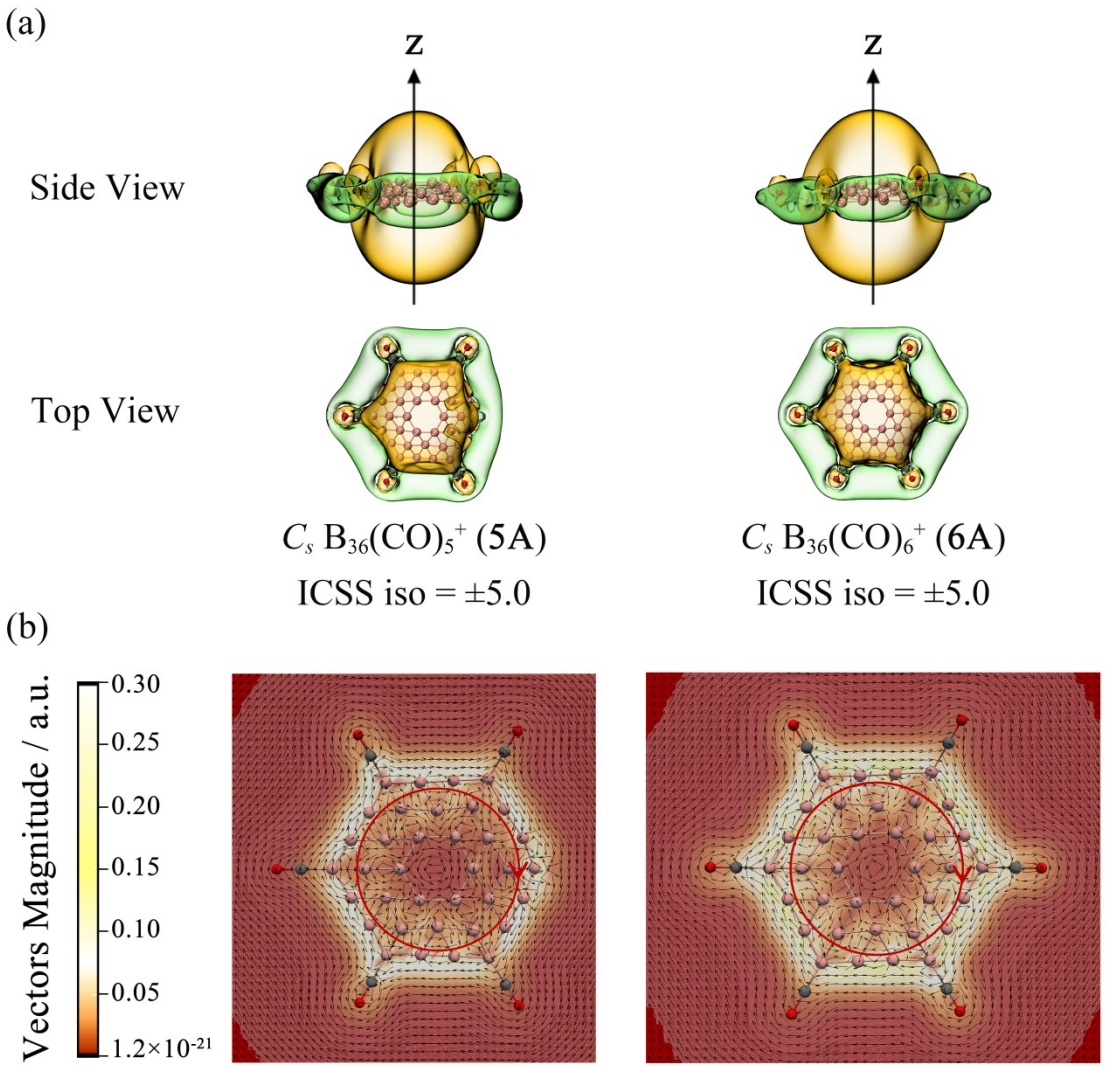

Fig.S29 (a) Calculated ICSS surfaces of C_s $B_{36}(CO)_5^+$ (**5A**), C_s $B_{36}(CO)_6^+$ (**6A**) at PBE0 level. Yellow and green regions stand for chemical shielding and de-shielding areas, respectively. (b) The corresponding calculated GIMIC plots 1.0 Å above the molecular planes, with the calculated ring current densities indicated in a.u. in the colour scale. The external magnetic field is perpendicular to the molecular plane. The red arrows represent directions of the ring currents on the GIMIC iso-surfaces.

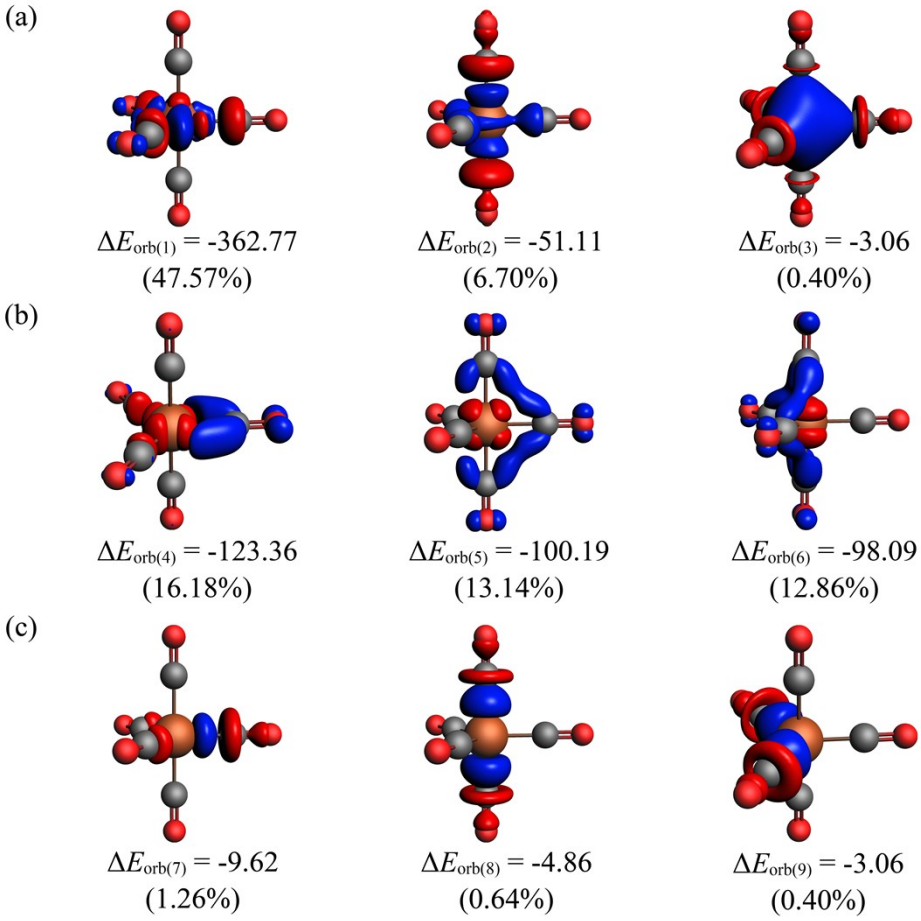

Fig.S30 Shape of the deformation densities $\Delta\rho_{(1)\text{-}(9)}$, which are associated with the orbital interaction energies ΔEorb (in kcal mol^{-1}) in $Fe(CO)_5$. The color code of the charge flow is red to blue.

Table S1. EDA-NOCV results for $B_{36}(CO)^+$ (**1A**) at the PBE0/TZ2P-ZORA level using PBE0/6-311+G(d) optimized geometries, with CO and B_{36}^+ designated as the interacting fragments. Energy values are given in kcal/mol.

Energy term	Assignment	Interacting fragment B_{36}^+ + CO
ΔE_{int}		-41.84
ΔE_{Pauli}		248.62
ΔE_{elstat}[a]		-117.88 (40.58%)
ΔE_{orb}[a]		-172.58 (59.42%)
$\Delta E_{orb}(1)$ [b]	$[B_{36}^+(p)] \leftarrow$ CO σ donation	-103.06 (59.72%)
$\Delta E_{orb}(2)$ [b]	$[B_{36}^+(p)] \rightarrow$ CO π backdonation	-32.32 (18.73%)
$\Delta E_{orb}(3)$ [b]	$[B_{36}^+(p)] \rightarrow$ CO π backdonation	-15.26 (8.84%)
ΔE_{orb} (rest) [b]		-21.94 (12.71%)

[a] The values in parentheses give the percentage contribution to the total attractive interactions $\Delta E_{elstat} + \Delta E_{orb}$. [b] The values in parentheses give the percentage contribution to the total orbital interactions ΔE_{orb}.

Table S2. EDA-NOCV results for B_{36}(CO) (**1a**) at the PBE0/TZ2P-ZORA level using PBE0/6-311+G(d) optimized geometries, with CO and B_{36} designated as the interacting fragments. Energy values are given in kcal/mol.

Energy term	Assignment	Interacting fragment B_{36} + CO
ΔE_{int}		-38.41
ΔE_{Pauli}		273.20
ΔE_{elstat}[a]		-129.72 (41.63%)
ΔE_{orb}[a]		-181.89 (58.37%)
$\Delta E_{orb}(1)$ [b]	[B_{36}(p)] ← CO σ donation	-100.42 (55.21%)
$\Delta E_{orb}(2)$ [b]	[B_{36}(p)] → CO π backdonation	-38.67 (21.26%)
$\Delta E_{orb}(3)$ [b]	[B_{36}(p)] → CO π backdonation	-16.78 (9.22%)
ΔE_{orb}(rest) [b]		-26.02 (14.31%)

[a] The values in parentheses give the percentage contribution to the total attractive interactions ΔE_{elstat}+ ΔE_{orb}. [b] The values in parentheses give the percentage contribution to the total orbital interactions $\Delta E_{orb.}$

Table S3. EDA-NOCV results for singlet D_{3h} symmetric $Fe(CO)_5$ complexes at the PBE0/TZ2P-ZORA level using PBE0/6-311+G(d) optimized geometries. The interacting fragments are the metal atom Fe in the singlet and $(CO)_5$ in the singlet state. Energy values are given in kcal/mol.

Energy term	Assignment	Interacting fragment $B_{36}^+ + CO$
ΔE_{int}		-276.38
ΔE_{Pauli}		1035.23
ΔE_{elstat}[a]		-548.99 (41.86%)
ΔE_{orb}[a]		-762.62 (58.14%)
$\Delta E_{orb}(1)$ [b]	[Fe(p)] ← $(CO)_5$ σ donation	-362.77 (47.57%)
$\Delta E_{orb}(2)$ [b]	[Fe(p)] ← $(CO)_5$ σ donation	-51.11 (6.7%)
$\Delta E_{orb}(3)$ [b]	[Fe(s)] ← $(CO)_5$ σ donation	-3.06 (0.40%)
$\Delta E_{orb}(4)$ [b]	[Fe(d)] → $(CO)_5$ π backdonation	-123.36 (16.18%)
$\Delta E_{orb}(5)$ [b]	[Fe(d)] → $(CO)_5$ π backdonation	-100.19 (13.14%)
$\Delta E_{orb}(6)$ [b]	[Fe(d)] → $(CO)_5$ π backdonation	-98.09 (12.86%)
$\Delta E_{orb}(7)$ [b]	$(CO)_5$ polarization	-9.62 (1.26%)
$\Delta E_{orb}(8)$ [b]	$(CO)_5$ polarization	-4.86 (0.64%)
$\Delta E_{orb}(9)$ [b]	$(CO)_5$ polarization	-3.06 (0.40%)
ΔE_{orb}(rest) [b]		-6.50 (0.85%)

[a] The values in parentheses give the percentage contribution to the total attractive interactions ΔE_{elstat}+ ΔE_{orb}. [b] The values in parentheses give the percentage contribution to the total orbital interactions ΔE_{orb}.